Applied Catalysis B: Environment and Energy 367 (2025) 125112

Contents lists available at ScienceDirect

Applied Catalysis B: Environment and Energy

journal homepage: www.elsevier.com/locate/apcatb

Ti-O-Mo bond-bridged PMA@MIL-125-NH_2 photocatalyst for gas acetone photocatalytic degradation

Shijie Yang [a,b], Xiao Wang [a], Guanqing Song [a,b], Guanhong Lu [a], Gansheng Shi [a], Yan Wang [a], Xiaofeng Xie [a], Jing Sun [a,*]

[a] State Key Lab of High Performance Ceramics and Superfine Microstructure, Shanghai Institute of Ceramics, Chinese Academy of Sciences, 585 Heshuo Road, Shanghai 201899, China

[b] University of Chinese Academy of Sciences, 19 (A) Yuquan Road, Beijing 100049, China

ARTICLE INFO

Keywords:
MIL-125-NH_2
Phosphomolybdic acid
Ti-O-Mo bond
Photocatalysis
Acetone

ABSTRACT

The effective generation and transfer of the photoelectrons are pivotal to the performance of photocatalysts. Herein, a novel Ti-O-Mo bond-bridged phosphomolybdic acid (PMA)@MIL-125-NH_2 composite was designed and synthesized for gas acetone photodegradation. PMA as a photoelectron reservoir was loaded in MIL-125-NH_2. The photogenerated electron transferred from the Ti_8-oxo cluster of MIL-125-NH_2 to PMA through the Ti-O-Mo bond configuration, which enhanced the photoelectrons storing ability of MIL-125-NH_2. Stored photoelectrons in PMA were effectively separated and released as $\bullet O_2^-$ by reacting with oxygen, while the amount of hole increased simultaneously. These holes and $\bullet O_2^-$ oxidized acetone subsequently. For PMA@MIL-125-NH_2, the degradation efficiency was 62 % for 400 ppm acetone, which was obviously higher than that of pristine MIL-125-NH_2 (45 % for 400 ppm acetone). Our results offered a promising method to improve the photogenerated carriers in metal-organic framework materials and improve their photocatalytic performance for VOCs degradation.

1. Introduction

Acetone is a common and well-known oxygen-containing volatile organic compounds (VOCs), mainly from many industries such as electronic equipment manufacturing, pharmaceuticals, textile dyeing and printing [1–3]. Due to its volatile and toxic characteristics, prolonged exposure to high levels of acetone could cause a variety of health problems in humans, such as headaches, narcosis, dizziness, and nausea [4,5]. Therefore, the development of effective removal strategies for acetone is of great importance for human health. Photocatalytic oxidation is regarded as an efficient technology for removing VOCs due to its eco-friendly and cost-effective feature [6,7], where the key of which lies in the selection and modification of photocatalysts [8,9].

MIL-125-NH_2 is a kind of Ti-based metal organic framework (MOF), which consists of Ti_8-oxo clusters as the secondary building unit (SBU) and 2-amino terephthalic acid as the ligand [10,11]. Compared with some typical photocatalysts, like metal oxide [12], metal sulfide [13], bismuth-based halogenated oxides [14] and g-C_3N_4 [15], MIL-125-NH_2 exhibited a large specific surface area with easily adjustable structure and abundant reactive sites [16]. The abundant and uniform porous structure of MIL-125-NH_2 facilitated the capture and diffusion of acetone [17]. Furthermore, the presence of Ti^{4+} endowed MIL-125-NH_2 with exceptional photocatalytic ability [18]. However, recent evidence demonstrated that MIL-125 can only accommodate up to 2 photoelectrons per SBU (Ti_8-oxo cluster) under photoexcitation [19]. Christopher et al. and Hyunho et al. further confirmed that this was related to the formation of Ti^{3+}-OH under light by using theoretical calculations [20,21]. The charge storage capacity of SBU in MIL-125 limited the excitation of photogenerated carriers [22]. Increasing the charge storage capacity of MIL-125 could be an effective way to boost the generation and migration of photogenerated carriers during photocatalysis.

Polyoxometalates (POMs) are discrete anionic clusters with multi-electron storage capability and can serve as a reservoir of photoelectrons [23,24]. Recently, Jiao et al. constructed two Ni_3PW_{10}@NU-1000 and $Ni_3P_2W_{16}$@NU-1000 for hydrogen generation [25]. The electrons stored in the Ni_3PW_{10} or $Ni_3P_2W_{16}$ component can be transferred to the active sites in the photocatalytic process and subsequently reduce protons to hydrogen [25]. Therefore, it might be possible that the incorporation of POMs into MIL-125-NH_2 could improve the charge storage capacity of MIL-125-NH_2. When considering the design and synthesis of

* Corresponding author.
E-mail address: jingsun@mail.sic.ac.cn (J. Sun).

https://doi.org/10.1016/j.apcatb.2025.125112
Received 17 November 2024; Received in revised form 15 January 2025; Accepted 28 January 2025
Available online 29 January 2025

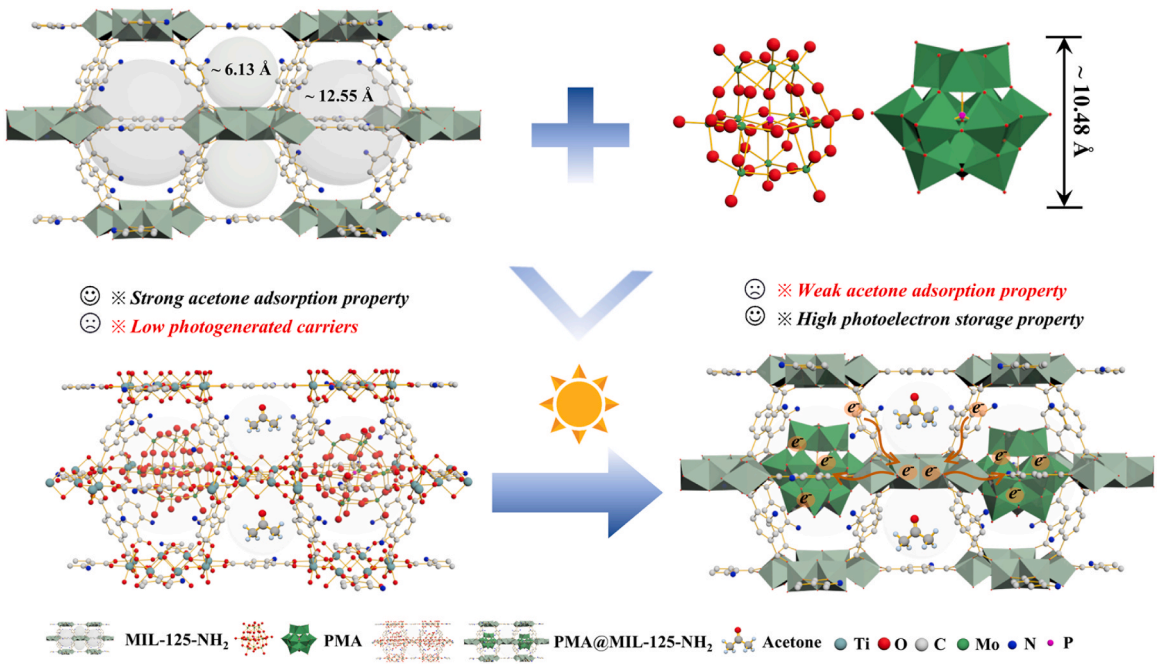

Scheme 1. Schematic illustration of design idea for PMA@MIL-125-NH_2 composite.

POM@MOF composites, the size of the POM is smaller than the pore of MOF, otherwise POM will be loaded on the surface of the MOF [26,27]. As shown in Scheme 1, there were two kinds of micropore structures in MIL-125-NH_2: octahedral cage (~12.55 Å) and tetrahedral cage (~6.13 Å) [10]. We selected phosphomolybdic acid (PMA, $H_3PMo_{12}O_{40}$) with an approximate size of 10.48 Å as the POMs component, which consisted of 12 molybdenum-oxygen octahedra around a phosphorus atom in the center [28]. PMA molecules were accommodated in the octahedral cage but did not enter into the tetrahedral cage. The tetrahedral cage of MIL-125-NH_2 was preserved for gas acetone capture and the diffusion of photodegradation products.

Inspired by the idea above, we successfully loaded PMA into MIL-125-NH_2 pore structure by impregnation method. The interaction and electron transfer between PMA and MIL-125-NH_2 were explored by the FTIR, XPS, ESR and CO-DRIFTs. The open-circuit voltage decay experiments showed that PMA as the reservoir of photoelectrons improved the charge storage capacity of MIL-125-NH_2 and these photoelectrons stored in the PMA can efficiently reduce absorbed oxygen to form $\bullet O_2^-$. The photocurrent curves, transient surface photovoltage spectra and PL spectra further showed the effect of improvement of charge storage capacity on the generation and separation of photoelectrons and holes. Finally, PTR-TOF-MS and GC-MS were used to explore the possible photocatalytic degradation pathway for acetone.

2. Experimental section

2.1. Materials

Titanium isopropoxide (TPOT), 2-aminoterephthalic acid (H_2ATA), N, N-dimethylformamide (DMF), ethanol, phosphomolybdic acid hydrate (PMA) and anhydrous methanol (MeOH) were purchased from Shanghai Adamas Reagent Co., Ltd. Acetic acid was purchased from China National Medicines Corporation Ltd. Deionized water for the experiment was produced by ultrapure water machine (Shanghai, Tondino Scientific Co., Ltd). All of the reagents were used without further purification.

2.2. Synthesis of photocatalysts

2.2.1. Synthesis of MIL-125-NH_2

MIL-125-NH_2 was synthesized by the solvothermal method. First, H_2ATA (3.1 mmol) was added to a mixture of DMF (36 mL), acetic acid (2.1 mL) and MeOH (4 mL). The mixture was sonicated for 30 min and transferred to a 100 mL Teflon liner. Then TPOT (2 mmol) was added into the container and heated at 150 °C for 24 h. The precipitate was washed by DMF and MeOH, and the MIL-125-NH_2 was obtained by vacuum drying at 80 °C for 6 h. Finally, the MIL-125-NH_2 was activated by vacuum drying at 150 °C for 12 h to remove the residual solvent molecules of the pore structure.

2.2.2. Synthesis of PMA@MIL-125-NH_2

100 mg MIL-125-NH_2 was added into MeOH (5 mL) and sonicated for 15 min. After that, 100 mg PMA was added into the above suspension and stirred for 24 h. The final suspension was centrifuged and washed with MeOH three times. The PMA@MIL-125-NH_2 was obtained by vacuum drying.

2.3. Characterization

The details of photocatalyst characterization were provided in Supporting information. In short, the characterization techniques were studied including powder X-ray diffraction (PXRD), Fourier transform infrared spectrometer (FTIR), thermogravimetry (TG), inductively coupled plasma optical emission spectrometer (ICP-OES), field emission scanning electron microscope (SEM), transmission electron microscope (TEM), X-ray photoelectron spectroscopy (XPS), UV-Vis diffuse reflectance spectra, nitrogen adsorption-desorption test, surface photovoltaic spectroscopy (SPS), photoluminescence spectroscopy (PL), temperature-programmed desorption (TPD), in-situ diffuse reflection infrared Fourier transform spectroscopy (DRIFTS), gas chromatography-mass spectrometry (GC-MS), time of flight mass spectrometer (PTR-TOF-MS), electron spin resonance spectroscopy (ESR).

2.4. Photoelectrochemical experiments

The photoelectrochemical experiments were carried out on the CHI

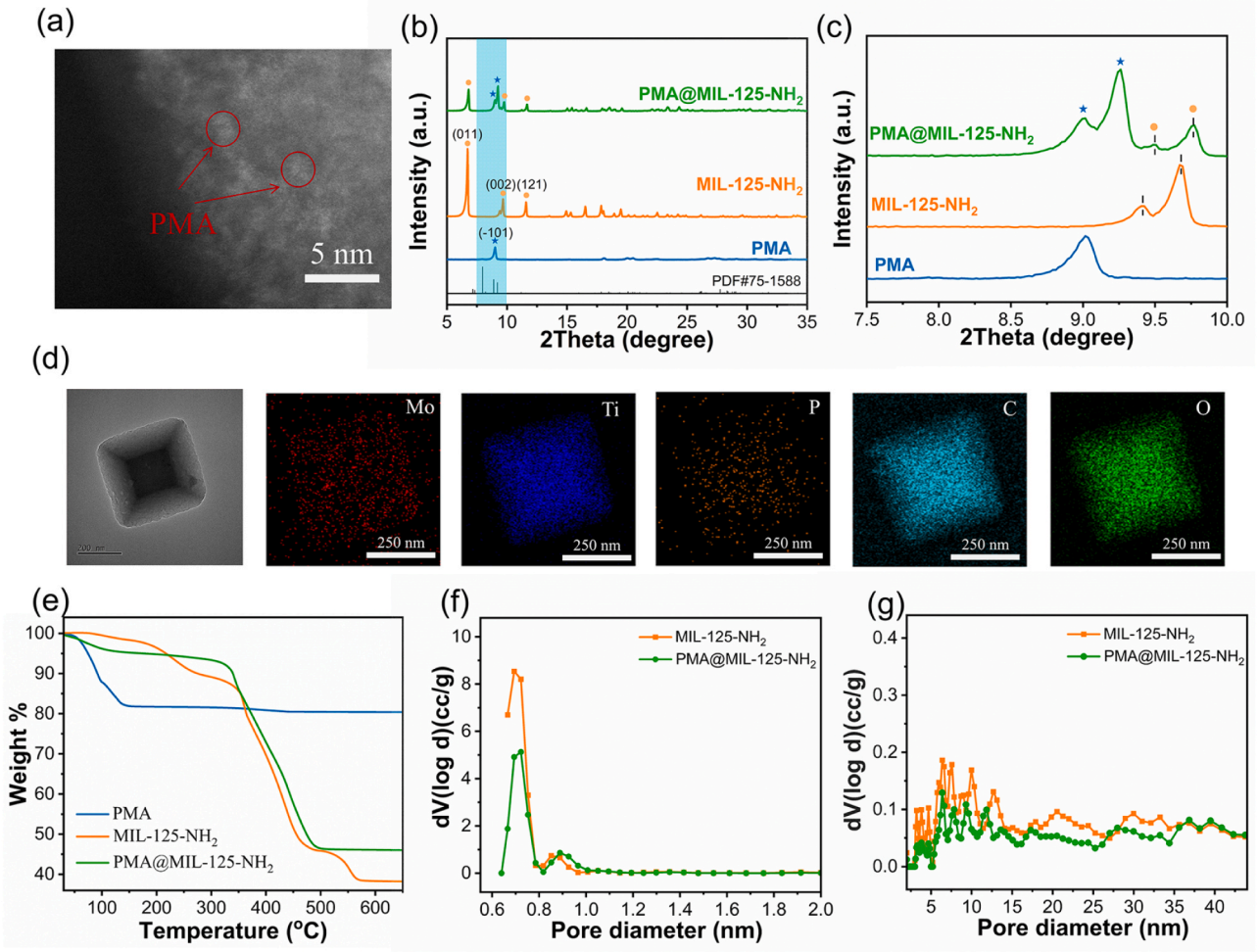

Fig. 1. (a) HAADF-STEM image of PMA@MIL-125-NH_2. (b) XRD spectra and (c) enlarged XRD spectra. (d) EDS-mapping images of Mo, Ti, P, C, N in PMA@MIL-125-NH_2. (e) TG curves, (f) micropore distribution and (g) pore distribution of photocatalysts.

650b (CH Instrument Company, Shanghai, China) electrochemical workstation equipped with a standard three-electrode system. 40 mg sample was dispersed in 2 mL ethanol to form the solution. Then, the 600 μl as-obtained solution was spin coating on the F-doped SnO_2-coating (FTO) glass sheet (2.5 mm × 1.5 mm). In a typical three-electrode system, the synthesized electrode (as-obtained FTO glass) serves as the working electrode, and the Ag/AgCl electrode and the platinum foil serve as the reference and counter electrode, respectively. All electrochemical experiments were measured in the Na_2SO_4 solution with a concentration of 0.5 mol/L.

2.5. Adsorption and photocatalysis experiments

The adsorption and photodegradation experiments were carried out in a gas-solid phase catalytic system as shown in Scheme S1[29]. 20 mg photocatalyst was dispersed in 2 mL ethanol and sonicated for 5 minutes. The obtained suspension was evenly coated on a glass pane (15 cm × 7.5 cm) and heated at 80 °C for 30 min to completely remove the ethanol. After that, the glass pane was put in the photocatalytic react chamber, and covered with a quartz plate. The air is generated through a three-in-one generator, passes through a humidification tank and then mixed with the target gases in a gas mixing device.

Acetone was selected as the target VOCs and its flow rate was 20 sccm for the adsorption and photocatalytic degradation. Xenon lamp, 30 cm above the reacting chamber, was used to emit light and the light intensity was 500 W (~ 22 mW/cm^2). The photocatalytic degradation experiment was started when the photocatalyst reached adsorption-desorption equilibrium under the dark condition. The concentrations of acetone were detected via gas chromatography. The adsorption capacity (A, mmol/g) of acetone was calculated by the following expression (1):

$$A = \frac{C_0 \cdot v}{M \cdot m}\left\{\left[\int_0^t \left(1-\frac{C}{C_0}\right)dt\right]_{\text{catalyst}} - \left[\int_0^t \left(1-\frac{C}{C_0}\right)dt\right]_{\text{blank}}\right\} \quad (1)$$

The photocatalytic degradation efficiency (η) of acetone was calculated according to the formula (2):

$$\eta = \left(1-\frac{C}{C_0}\right) \times 100\% \quad (2)$$

The kinetic process of photocatalytic degradation was simulated via a pseudo-first-order reaction, which conformed to the following Eq. (3):

$$\ln\left(\frac{C}{C_0}\right) = -kt \quad (3)$$

Where C_0 represents the initial concentration of acetone, C represents the actual concentrations of acetone in the mixing gas, v represents the flow rate of acetone, M and m represent the molar mass of acetone and the quality of photocatalysts, respectively. The t represents the actual time and k represents the kinetic constants of the photocatalytic degradation.

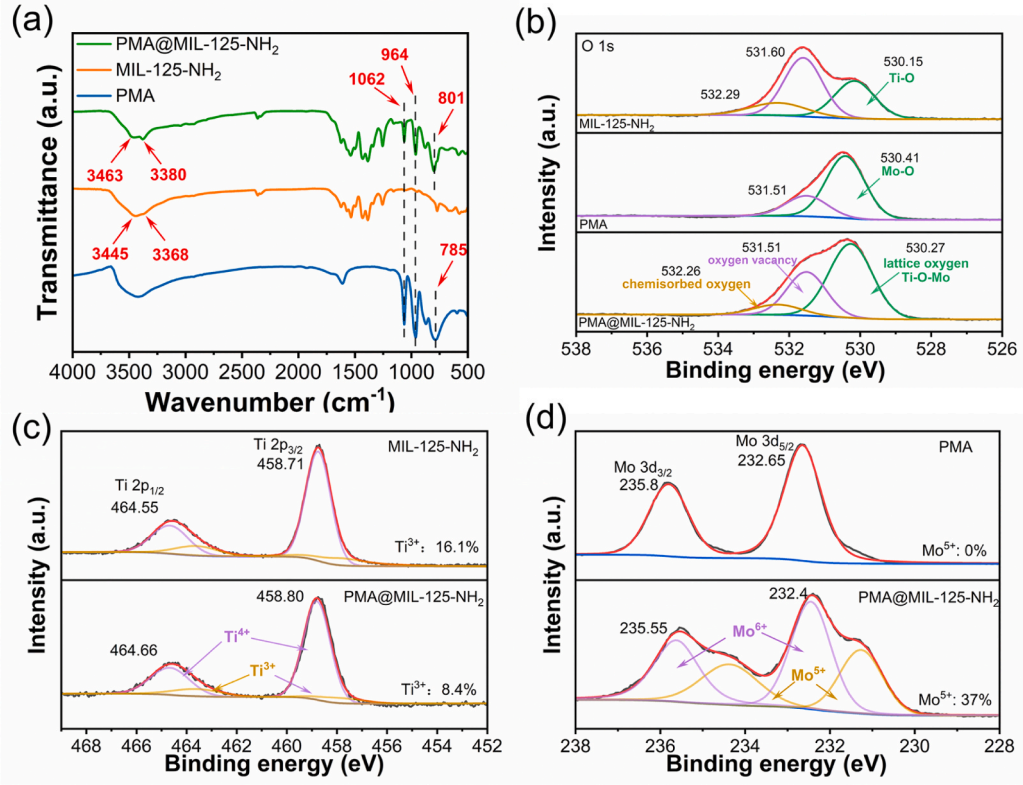

Fig. 2. (a) FTIR spectra of photocatalysts. XPS spectra of photocatalysts of (b) O, (c) Ti and (d) Mo.

3. Result and discussion

3.1. Characterization of photocatalysts

The pristine MIL-125-NH_2 was synthesized by solvothermal methods [30]. It was then impregnated in the methanol solution containing PMA to obtain the PMA@MIL-125-NH_2 composite. According to the image of HAADF-STEM (Fig. 1a), PMA molecules were loaded successfully in the PMA@MIL-125-NH_2. The results of scanning electron microscopy (SEM) and transmission electron microscope (TEM) indicated that the morphology of MIL-125-NH_2 was almost unchanged after loading PMA, which exhibited the polyhedron morphology (Fig. S1 and Fig. S2). The elemental distribution of PMA@MIL-125-NH_2 was detected by the EDS-mapping. As shown in Fig. 1d, Mo, Ti, P, C and O were homogeneously dispersed in the MIL-125-NH_2, revealing that the PMA was loaded evenly in MIL-125-NH_2. This favored the coordinative linkage between PMA and MIL-125-NH_2. As determined by inductively coupled plasma optical emission spectrometer (ICP-OES), the Mo and Ti content of PMA@MIL-125-NH_2 were 21.05 % and 11.66 %, respectively, namely the actual mass ratio of PMA and MIL-125-NH_2 in PMA@-MIL-125-NH_2 was approximately 0.66/1.

Powder X-ray diffraction (XRD) patterns were used to characterize the crystal phase of photocatalysts. The diffraction peaks of PMA and MIL-125-NH_2 simultaneously appeared in the PMA@MIL-125-NH_2 (Fig. 1b), indicating that PMA retained the Keggin-type structure. The diffraction peak at 9.2°, which was assigned to the (-1, 0, 1) facet of PMA (PDF#75-1588), shifted to 9.7° implying the strong interaction between PMA and MIL-125-NH_2 (Fig. 1c). The thermogravimetric analyses (TG) were used to investigate the thermal stability of photocatalysts (Fig. 1e). The weight loss at around 250 °C of MIL-125-NH_2 was attributed to the evaporation of DMF [31]. The residual mass of PMA@MIL-125-NH_2 was higher than that of MIL-125-NH_2, revealing that PMA was successfully loaded in MIL-125-NH_2. The physical structure properties of photocatalysts were characterized by N_2 adsorption-desorption isotherms (Fig. S5). The BET value decreased from 1345 m^2/g to 901.4 m^2/g after loading PMA, together with a reduction in the volume of both micropore and mesopore in PMA@MIL-125-NH_2 compared to pristine MIL-125-NH_2 (Fig. 1f and g), which indicated that PMA was successfully loaded in the pores of MIL-125-NH_2.

The structure of photocatalysts was further characterized by FTIR spectrum (Fig. 2a). The bands at 3463, 3380, 1062, 964 and 801 cm^{-1} of PMA@MIL-125-NH_2 were assigned to $\nu_s(NH_2)$, $\nu_{as}(NH_2)$, ν_{as}(P-O), ν_{as}(Mo═O) and ν_{as}(Mo-O), respectively [31,32]. The appearance of these peaks showed that PMA was successfully loaded in the MIL-125-NH_2 and maintained the Keggin structure. Besides, the ν_{as}(-Mo-O) of the PMA exhibited a blue shift after PMA was loaded in MIL-125-NH_2, implying the plausible connection between PMA and MIL-125-NH_2 through the Ti-O-Mo bonds. To further validate the interfacial Ti-O-Mo bond between PMA and MIL-125-NH_2, the electronic structure of the composite was disclosed by X-ray photoelectron spectroscopy (XPS). As shown in Fig. 2b, the O 1s peaks at 532.29, 531.60 and 530.16 eV of MIL-125-NH_2 belonged to chemisorbed oxygen, oxygen vacancy and lattice oxygen (Ti-O bond), respectively [33,34]. The binding energy of lattice oxygen in PMA@MIL-125-NH_2 was higher than that of MIL-125-NH_2 (Ti-O bond) and lower than that of PMA (Mo-O bond), corresponding to the formation of Ti-O-Mo bond [35]. The amount of oxygen vacancy in PMA@MIL-125-NH_2 was also higher than PMA but lower than MIL-125-NH_2, which implied that the partial oxygen atoms of PMA embedded in the oxygen vacancy of MIL-125-NH_2 to form the interfacial Ti-O-Mo bond. This result also corresponded to the result of FTIR (Fig. 2a). The Mo 3d peaks at 235.8 and 232.65 eV for PMA were attributed to Mo $3d_{3/2}$ and $3d_{5/2}$, respectively (Fig. 2d). The characteristic peak of Mo^{5+} (231.27 eV) appeared obviously in PMA@MIL-125-NH_2, indicating that partial Mo^{6+} of PMA got electrons and was reduced as Mo^{5+} [32]. The Ti 2p peaks at 464.55 and 458.71 eV for MIL-125-NH_2 belonged to Ti $2p_{1/2}$ and $2p_{3/2}$, respectively (Fig. 2c). The content of Ti^{3+} (463.60 eV and 457.78 eV) decreased after loading PMA, disclosing that partial Ti^{3+} lost electrons and was oxidized as Ti^{4+}

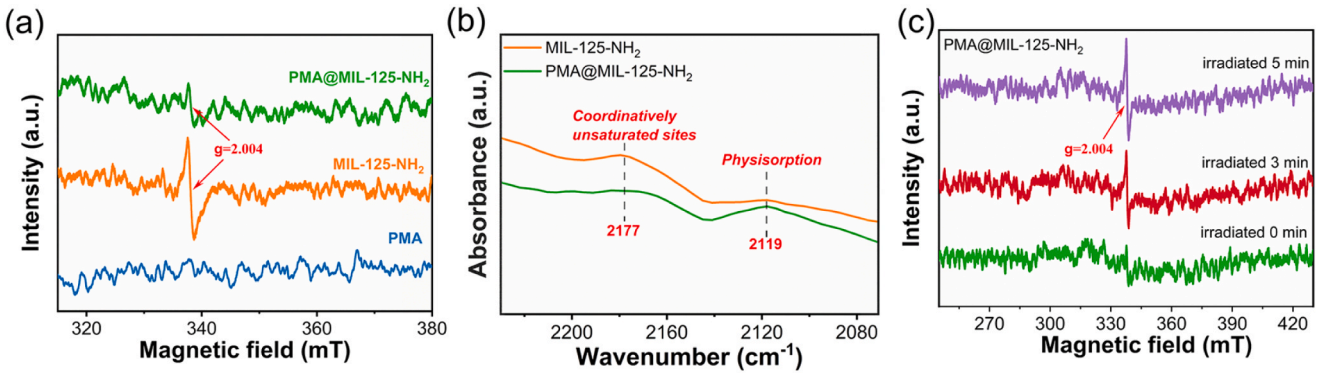

Fig. 3. (a) ESR spectra of photocatalysts in the dark. (b) CO-DRIFTs spectra of photocatalysts. (c) ESR spectra of PMA@MIL-125-NH_2 at the different irradiation times.

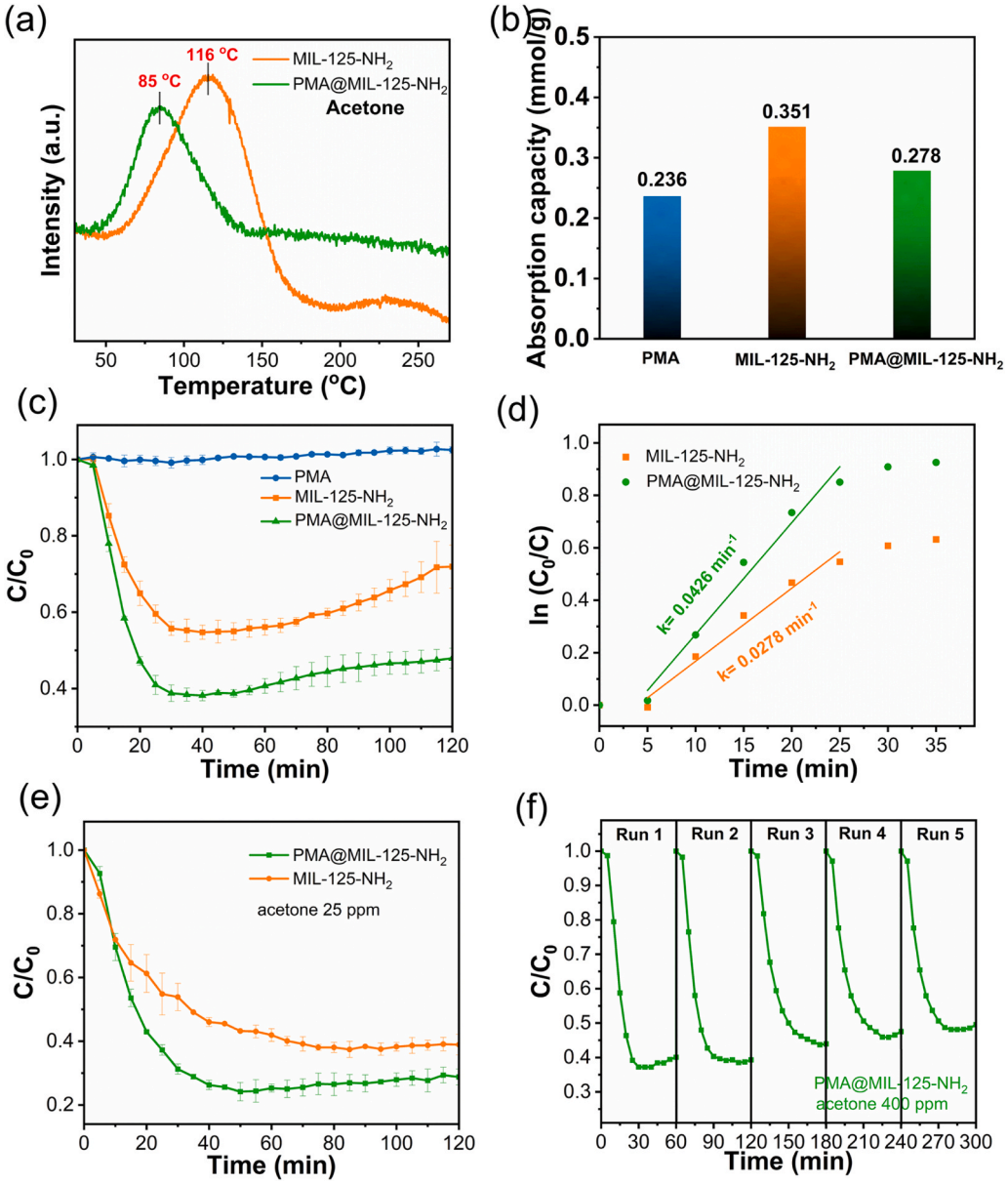

Fig. 4. (a) Acetone-TPD plots of photocatalysts. (b) Adsorption capacity of photocatalysts. (c) Photodegradation curves for 400 ppm acetone and (d) corresponding kinetic curves. (e) Photodegradation curves for 25 ppm acetone on photocatalysts. (f) Degradation curves for 400 ppm acetone on PMA@MIL-125-NH_2 with 5 cycles.

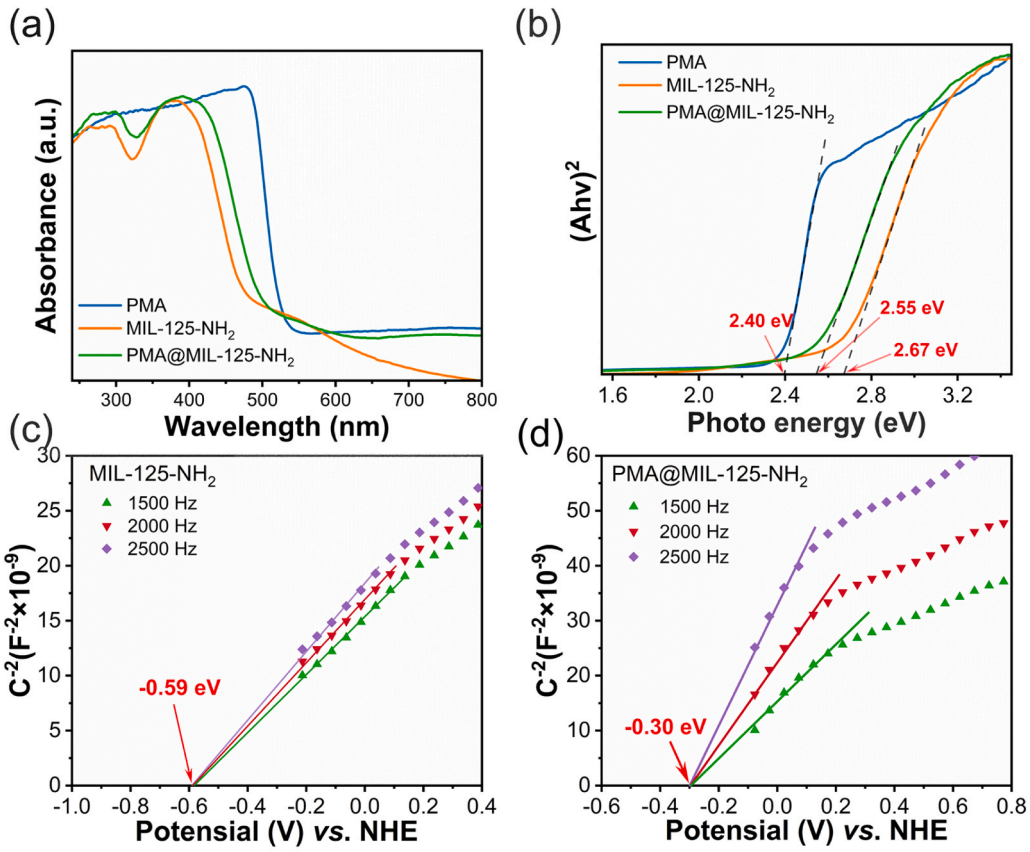

Fig. 5. (a) UV–VIS spectra and (b) corresponding Tauc plots of photocatalysts. Mott-Schottky curves of (c) MIL-125-NH_2 and (d) PMA@MIL-125-NH_2.

[33]. Therefore, it can be determined that the formation of the interfacial Ti-O-Mo bond led to the electron transfer from Ti of MIL-125-NH_2 to Mo of PMA, which possibly was attributed to the stronger electronegativity of Mo than that of Ti. Besides, this electron transfer can take full advantage of the property of storing multielectrons of PMA and improve the ability to store photogenerated carriers [36]. The P 2s peak was almost unchanged (Fig. S6a), indicating that the internal structure of PMA was unchanged and retained the Keggin-type structure. The N 1s peak overlapped with Mo 3p peak and it was difficult to clearly analyze the state changes of N atoms (Fig. S6b).

The ESR spectrum was used to further verify the formation of the Ti-O-Mo bond. As shown in Fig. 3a, the free electrons signal caused by oxygen vacancy (g = 2.004) of MIL-125-NH_2 decreased after loading PMA [37], which further implied that the formation of the Ti-O-Mo bond resulted from the embedding of oxygen atoms in PMA with oxygen vacancies in MIL-125-NH_2. Moreover, the CO-DRIFTs spectrum was used to detect the unsaturated Ti^{3+} sites [38]. As shown in Fig. 3b, the band at 2177 cm^{-1} of MIL-125-NH_2 was attributed to the adsorption of CO on the unsaturated metal sites (Ti^{3+}) and its intensity was decreased meaning that the amount of Ti^{3+} was decreased after loading PMA [39, 40]. This manifested that the Ti^{3+} lost electrons and formed Ti^{4+} ($Ti^{3+} \rightarrow Ti^{4+} + e^-$). The electron transferred to Mo of PMA through the Ti-O-Mo bond, which made Mo^{6+} get an electron and formed Mo^{5+} ($Mo^{6+} + e^- \rightarrow Mo^{5+}$). Besides, the free electrons signal under light irradiation of PMA@MIL-125-NH_2 was enhanced with irradiated time (Fig. 3c), indicating the accumulation of photoelectrons and their efficient transfer in PMA@MIL-125-NH_2.

3.2. Photodegradation performance

To simulate the actual environment, both adsorption and photodegradation acetone experiments were conducted in a gas-solid mobile phase reaction system (Scheme S1). The adsorption property of photocatalysts for acetone was tested first by the acetone-TPD. As shown in Fig. 4a, the intensity of the acetone desorption peak of MIL-125-NH_2 was higher than that of PMA@MIL-125-NH_2, disclosing that pristine MIL-125-NH_2 exhibited good adsorption performance. The dynamic adsorption experiments were conducted (Fig. S7) and the corresponding acetone adsorption capacities of PMA, MIL-125-NH_2 and PMA@MIL-125-NH_2 were calculated to 0.236, 0.351 and 0.278 mmol/g, respectively (Fig. 4b). The dynamic photodegradation curves of 400 ppm acetone were shown in Fig. 4c. The photodegradation efficiency of acetone was 45 % and 62 % on MIL-125-NH_2 and PMA@MIL-125-NH_2, respectively, and no degradation for PMA. Furthermore, as shown in Fig. 4d, PMA@MIL-125-NH_2 exhibited a higher kinetic constant (0.0426 min^{-1}) compared to that of MIL-125-NH_2 (0.0278 min^{-1}). These manifested that the load of PMA improved the photocatalytic degradation efficiency of MIL-125-NH_2 for acetone. We also tested the photodegradation of acetone with low concentration (25 ppm). The efficiency was increased from 64 % for MIL-125-NH_2 to 78 % for PMA@MIL-125-NH_2, which showed that the load of PMA can effectively enhance the photocatalytic performance of MIL-125-NH_2 for acetone both at high and low concentrations. Besides, the photocatalytic degradation efficiency of PMA@MIL-125-NH_2 for 400 ppm acetone was higher than that of commercial P25 (Fig. S8). To evaluate the stability of the photocatalysts, we performed five cyclic degradation tests with PMA@MIL-125-NH_2. The photodegradation efficiency for acetone was 53 % for the fifth cycle (Fig. 4f) and the XRD patterns and FTIR spectra were kept almost the same after 5 cycles (Fig. S9). These indicated that the PMA@MIL-125-NH_2 have good stability for photocatalytic degradation acetone.

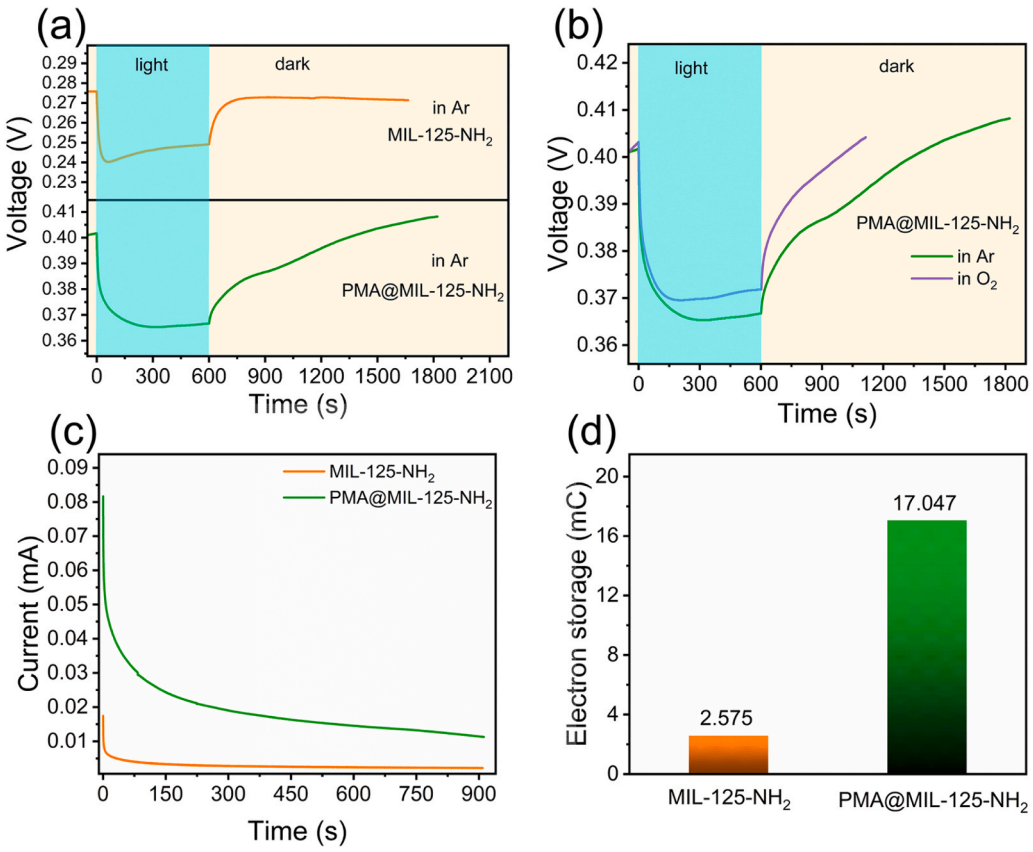

Fig. 6. Open-circuit voltage decay of MIL-125-NH_2 and PMA@MIL-125-NH_2 under argon atmosphere. (b) Open-circuit voltage decay of PMA@MIL-125-NH_2 under different atmospheres. (c) The discharge curves and (d) calculated electron storage of MIL-125-NH_2 and PMA@MIL-125-NH_2 after 600 s irradiation.

3.3. Photoelectrochemical properties of PMA@MIL-125-NH_2

To analyze the role of PMA, the optical absorption properties of the photocatalysts were investigated at first by the UV–vis spectra. PMA enhanced the absorption ability of MIL-125-NH_2 (Fig. 5a). The bandgaps of PMA, MIL-125-NH_2 and PMA@MIL-125-NH_2 were 2.40, 2.67 and 2.55 eV, respectively (Fig. 5b). Moreover, Mott-Schottky curves of both MIL-125-NH_2 and PMA@MIL-125-NH_2 showed the characteristics of n-type semiconductors (Fig. 5c and d). The CB values of MIL-125-NH_2 and PMA@MIL-125-NH_2 were −0.59 and −0.30 eV, respectively. Combined with the results of bandgaps, the VB values of MIL-125-NH_2 and PMA@MIL-125-NH_2 were calculated to be 2.08 and 2.25 eV, respectively (VB – CB = bandgap). The load of PMA elevated the position of VB (from 2.08 eV to 2.25 eV), which indicated that PMA@MIL-125-NH_2 exhibited a stronger oxidizing ability compared to pristine MIL-125-NH_2.

Upon excitation by light, electrons in MIL-125-NH_2 can be excited from the ligand to the Ti-oxo clusters (LMCT, ligand-to-metal charge transfer)[41]. However, the Ti-oxo cluster in MIL-125 was capable of storing a maximum of only two photoelectrons [19], limiting the excitation of photoelectrons [21,22]. Considering that PMA showed the property of storing multielectrons [42], it was rational to infer that the role of PMA was to improve the storage capacity of MIL-125-NH_2 for photogenerated carriers and further to increase the amounts of photoelectrons. To validate our point, open-circuit voltage decay (OCVD) was measured for MIL-125-NH_2 and PMA@MIL-125-NH_2 under argon atmosphere [43,44]. As shown in Fig. 6a, the open-circuit voltage of both MIL-125-NH_2 and PMA@MIL-125-NH_2 displayed a decrease under light excitation, corresponding to the n-type characteristic of semiconductors [44]. Under light irradiation, the open-circuit voltage of MIL-125-NH_2 was immediately maximal, whereas the open-circuit voltage of PMA@MIL-125-NH_2 reached its maximum after 300 s of light irradiation. This behavior demonstrated a noticeable accumulation of photoelectrons in PMA@MIL-125-NH_2. Moreover, the open-circuit voltage of MIL-125-NH_2 was partially recovered during the light irradiation, implying the severe electron-hole recombination in MIL-125-NH_2. After 600 s of photoexcitation, the open-circuit voltage of MIL-125-NH_2 was quickly returned to its initial potential within 150 s, while the recovery of the open-circuit voltage of PMA@MIL-125-NH_2 spanned over 1000 s. This was the powerful illustration that the photoelectrons can be transferred and stored in PMA. To further prove that these stored photoelectrons can be released efficiently, open-circuit voltage decay of PMA@MIL-125-NH_2 was measured under oxygen atmosphere. As shown in Fig. 6b, the open-circuit voltage of PMA@MIL-125-NH_2 in oxygen was smaller than that in argon and the open-circuit voltage decays faster in oxygen than in argon, indicating that these photoelectrons stored in PMA@MIL-125-NH_2 can be efficiently released ($O_2 + e^- \rightarrow \bullet O_2^-$). To determine the release quantity of photoelectrons, the electrochemical discharge test of the photocatalyst was performed as shown in Fig. 6c. The amount of discharge of the photocatalysts can be obtained by integrating the discharge current (Fig. 6d) [44]. The PMA@MIL-125-NH_2 released 17.047 mC electrons after 600 s of photo-charging, which was much higher than that of MIL-125-NH_2 (2.575 mC).

In order to confirm that the improvement of the photoelectron storage capacity of MIL-125-NH_2 could facilitate the excitation of photoelectrons, the photocurrent experiment. As shown in Fig. 7a, the intensity of photocurrent was enhanced after loading PMA, indicating the increase of photogenerated carriers. The surface transient photovoltage spectra were conducted to further investigate the generation of photogenerated carriers [45]. As shown in Fig. 7b, the surface photovoltage value of PMA@MIL-125-NH_2 was obviously higher than pristine

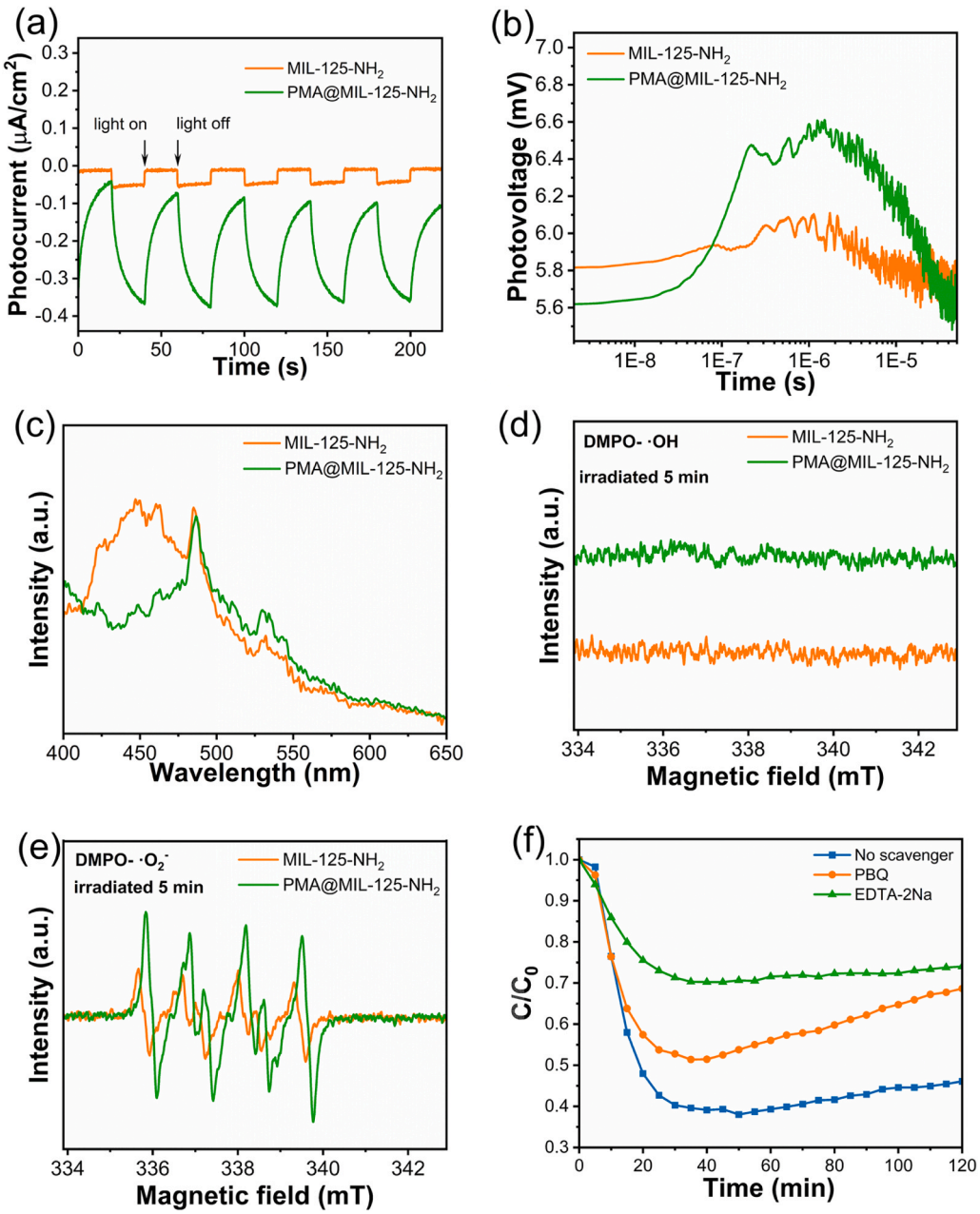

Fig. 7. (a) The transient photocurrent curves of photocatalysts. (b) Transient surface photovoltage spectra of photocatalysts at 355 nm test wavelength. (c) PL spectra of photocatalysts excited at 350 nm. DMPO spin-trapping ESR spectra for (d) •OH and (e) $•O_2^-$ of MIL-125-NH_2 and PMA@MIL-125-NH_2. (f) The degradation curves of PMA@MIL-125-NH_2 for 400 ppm acetone with scavengers.

MIL-125-NH_2, demonstrating that the load of PMA exhibited a significant promoting effect on the generation of photogenerated carriers. These results manifested that the improvement of the photoelectron storage capacity of MIL-125-NH_2 enhanced the amounts of photoelectron. Furthermore, storing photoelectrons in PMA effectively suppressed the recombination of photoelectrons with holes, which was verified by the result of Photoluminescence (PL) spectra. As shown in Fig. 7c, much weaker PL intensity was observed in the PMA@MIL-125-NH_2 compared with pristine MIL-125-NH_2, confirming that the electron-hole recombination was effectively suppressed after loading PMA.

Holes, $•O_2^-$ and •OH were the important reactive species during the photodegradation of VOCs [46]. To further ascertain whether photoelectrons stored in PMAs can be efficiently utilized during the photocatalysis, the change in reactive species during the photocatalysis was explored. 5,5-dimethyl-1-pyrroline N-oxide (DMPO) was used as a spin trap reagent to detect the generation of $•O_2^-$ and •OH radicals by ESR spectrum [47]. No •OH radicals were detected in either MIL-125-NH_2 or PMA@MIL-125-NH_2 (Fig. 7d) and the amount of $•O_2^-$ radicals increased after loading PMA (Fig. 7e). The increase of $•O_2^-$ radicals after loading PMA disclosed that the photoelectrons stored in PMAs can be efficiently released, which corresponding to the results of Fig. 6b ($O_2 + e^- \rightarrow •O_2^-$). Besides, since no •OH radicals were detected, it can be reasonably inferred that the main reactive species were holes and $•O_2^-$ radicals during the photodegradation. To validate this, the reactive species scavenging experiment was conducted on PMA@MIL-125-NH_2. PBQ (p-Benzoquinone) was used to scavenge $•O_2^-$ and EDTA-2Na (Ethylenediaminetetraacetic acid disodium salt) was used to scavenge holes. The addition of PBQ resulted in a reduction of the acetone degradation efficiency from 62 % to 49 % by quenching $•O_2^-$, and the addition of EDTA-2Na led to a decline in the degradation efficiency from 62 % to

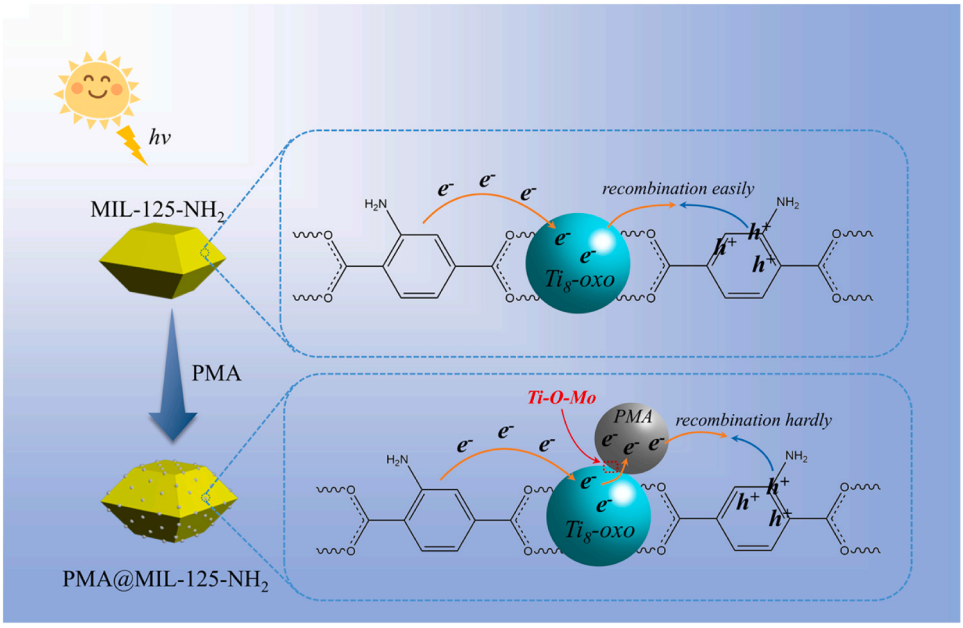

Fig. 8. Schematic illustration of the interaction mechanism between PMA and MIL-125-NH_2.

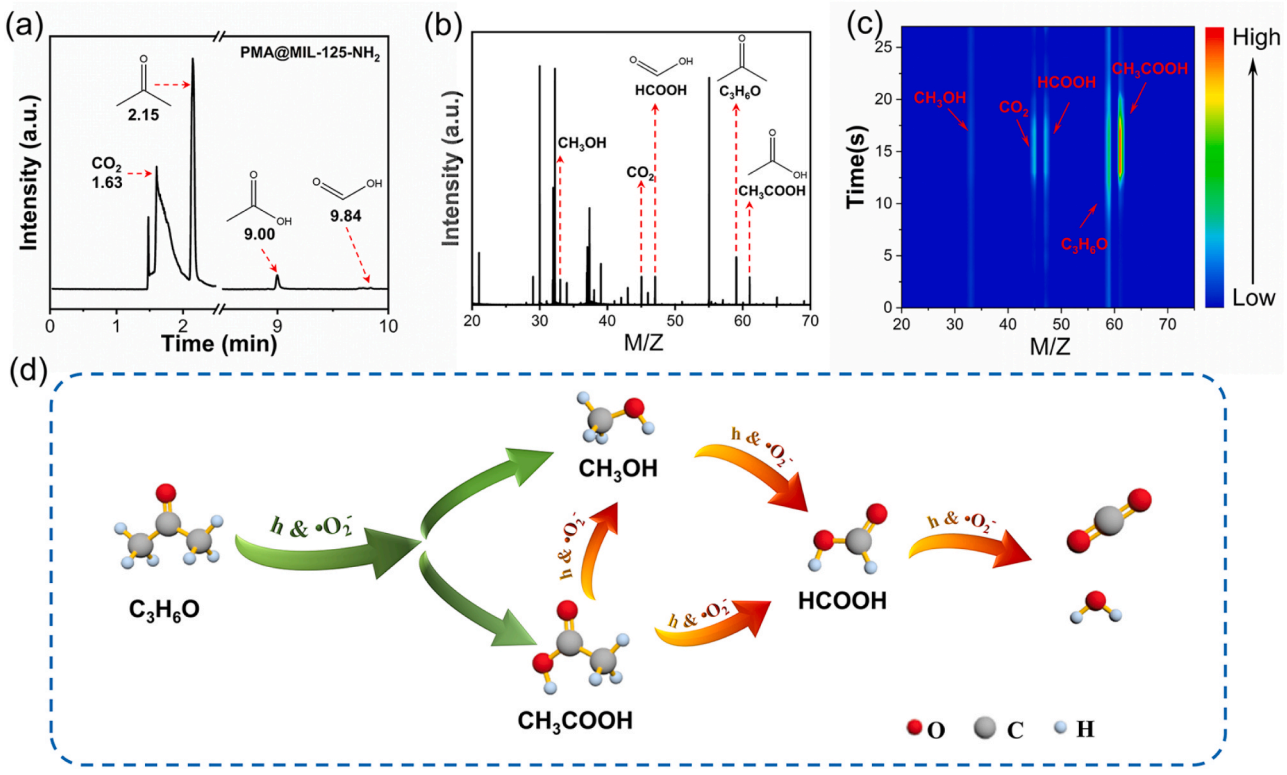

Fig. 9. (a) GC-MS data of acetone photodegradation of PMA@MIL-125-NH_2. PTR-TOF-MS (b) spectra and (c) trace of PMA@MIL-125-NH_2 for acetone photodegradation. (d) Photodegradation pathway of acetone on PMA@MIL-125-NH_2.

30 % by quenching holes (Fig. 7f). These implied that both holes and $\bullet O_2^-$ radicals had an important role during photodegradation.

Based on the above results, we proposed a possible interaction mechanism between PMA and MIL-125-NH_2 as shown in Fig. 8. Upon light absorption, the electrons in the ligand will be excited to the Ti_8-oxo cluster by ligand-to-metal charge transfer (LMCT). After loading PMA, the interfacial Ti-O-Mo bond served as an "electron bridge", ensuring the efficient transfer and storage of electrons from the Ti_8-oxo cluster of MIL-125-NH_2 to PMA. On the one hand, stored photoelectrons in PMA boosted the amounts of photoelectrons that can be excited to generate more photogenerated carriers. On the other hand, storing photoelectrons in PMA suppressed the recombination of photoelectrons with holes in MIL-125-NH_2. Therefore, the PMA@MIL-125-NH_2 exhibited a better photocatalytic degradation performance for acetone.

3.4. Photodegradation mechanism for acetone

The analysis of intermediates was important for the study of the degradation process for acetone. To explore the photodegradation of acetone on PMA@MIL-125-NH_2, gas chromatography-mass spectrometry (GC-MS) was used to detect the intermediate species of acetone on photocatalysts during the photodegradation. As shown in Fig. 9a, three major intermediate species were identified by GC-MS during the degradation of acetone, namely CO_2, acetic acid and formic acid. Additionally, we used the proton-transfer-reaction time-of-flight mass spectrometer (PTR-TOF-MS) to detect the intermediate species of acetone in flowing gas during the photodegradation [48]. As shown in Fig. 9b, the peaks at 30.01, 32.00 and 45.99 M/Z were assigned to the nitric oxide, oxygen and nitrogen dioxide in the drift-tube of PTR-TOF-MS, respectively. The peaks at 37.02 and 55.04 M/Z were attributed to the water cluster. The peaks at 33.02, 45.01, 47.01, 59.05 and 61.03 M/Z were assigned to methanol, carbon dioxide, formic acid, acetone and acetic acid, respectively. The information on peaks of PTR-TOF-MS was summarized in Table. S4. Compared to the PTR-TOF-MS results of pristine MIL-125-NH_2 (Fig. S10b), we detected large amounts of acetic acid during the degradation of acetone with PMA@MIL-125-NH_2 (Fig. 9c). This implied that the load of PMA promoted the formation of acetic acid during the photodegradation.

Combining the results of GC-MS and PTR-TOF-MS, we proposed a possible photodegradation mechanism for acetone. Under light irradiation, the photocatalysts generated the electrons and holes through ligand-to-metal charge transfer mechanism (formula (4)) [49]. The excited electrons interacted with O_2 to form $\bullet O_2^-$ (formula (5)). Firstly, acetone was dissociative to form methanol and acetic acid species in the presence of holes and $\bullet O_2^-$ (formula (6)). The generated acetic acid was oxidized as methanol and formic acid (formula (7)). Then, methanol was rapidly oxidized to formic acid (formula (8)). The formic acid was finally oxidized to CO_2 and H_2O (formula (9)).

$$photocatalyst \xrightarrow[h\nu]{LMCT} e^- + h^+ \quad (4)$$

$$e^- + O_2 \rightarrow \cdot O_2^- \quad (5)$$

$$C_3H_6O \xrightarrow{\cdot O_2^-\ h^+} CH_3COOH + CH_3OH \quad (6)$$

$$CH_3COOH \xrightarrow{\cdot O_2^-\ h^+} CH_3OH + HCOOH \quad (7)$$

$$CH_3OH \xrightarrow{\cdot O_2^-\ h^+} HCOOH \quad (8)$$

$$HCOOH \xrightarrow{\cdot O_2^-\ h^+} CO_2 + H_2O \quad (9)$$

4. Conclusion

In conclusion, we successfully loaded PMA into the pore structure of MIL-125-NH_2 by impregnation method to form PMA@MIL-125-NH_2 composite. The photoelectrons can be transferred from Ti-oxo clusters of MIL-125-NH_2 to PMA through interfacial Ti-O-Mo bond and stored in PMA. This enhanced the amounts of photoelectrons that can be excited and generated more holes. Additionally, the photoelectrons stored in PMA can be efficiently reacted with oxygen as $\bullet O_2^-$ radicals. For PMA@MIL-125-NH_2, the degradation efficiency was 62 % for 400 ppm acetone, which was obviously higher than that of pristine MIL-125-NH_2 (45 %). Finally, we proposed a possible photodegradation mechanism for acetone by using GC-MS and PTR-TOF-MS. This work provided a promising approach to promote the photogenerated carriers in MOF materials, and a strategy for the design of high-performance photocatalysts for VOCs.

Declaration of Competing Interest

The authors declare that they have no known competing financial interests or personal relationships that could have appeared to influence the work reported in this paper

Acknowledgments

This work was financially supported by the National Natural Science Foundation of China (52072387)

Appendix A. Supporting information

Supplementary data associated with this article can be found in the online version at doi:10.1016/j.apcatb.2025.125112.

Data availability

Data will be made available on request.

References

[1] C. He, J. Cheng, X. Zhang, M. Douthwaite, S. Pattisson, Z. Hao, Recent advances in the catalytic oxidation of volatile organic compounds: a review based on pollutant sorts and sources, Chem. Rev. 119 (2019) 4471–4568, https://doi.org/10.1021/acs.chemrev.8b00408.
[2] M. Wen, W. Deng, J. Huang, S. Zhang, Q. Lin, C. Wang, S. Ma, W. Wang, X. Zhang, G. Li, T. An, Atmospheric VOCs in an industrial coking facility and the surrounding area: Characteristics, spatial distribution and source apportionment, J. Environ. Sci. 138 (2024) 660–670, https://doi.org/10.1016/j.jes.2023.04.026.
[3] Y. Zheng, Q. Liu, C. Shan, Y. Su, K. Fu, S. Lu, R. Han, C. Song, N. Ji, D. Ma, Defective ultrafine MnO_x nanoparticles confined within a carbon matrix for low-temperature oxidation of volatile organic compounds, Environ. Sci. Technol. 55 (2021) 5403–5411, https://doi.org/10.1021/acs.est.0c08335.
[4] Y. Zheng, W. Xu, J. Yang, C. Shan, Y. Wang, R. Han, G. Zang, Q. Liu, Catalytic oxidation of VOCs and CO on cobalt-based materials: strategies and mechanisms for improving activity and stability, Chem. Eng. J. 484 (2024) 149296, https://doi.org/10.1016/j.cej.2024.149296.
[5] L. Zhang, X. Li, H. Chen, Z. Wu, M. Hu, M. Yao, Haze air pollution health impacts of breath-borne VOCs, Environ. Sci. Technol. 56 (2022) 8541–8551, https://doi.org/10.1021/acs.est.2c01778.
[6] P. Haghighi, F. Haghighat, TiO2-based photocatalytic oxidation process for indoor air VOCs removal: a comprehensive review, Build. Environ. 249 (2024) 111108, https://doi.org/10.1016/j.buildenv.2023.111108.
[7] H. Zhang, Z. Wang, L. Wei, Y. Liu, H. Dai, J. Deng, Recent progress on VOC pollution control via the catalytic method, Chin. J. Catal. 61 (2024) 71–96, https://doi.org/10.1016/S1872-2067(24)60043-4.
[8] S. Lu, X. Yao, Y. Cheng, L. Zhao, Recent developments and challenges for volatile organic compounds control by the synergistic of adsorption and photocatalysis, Appl. Catal. O: Open 193 (2024) 206975, https://doi.org/10.1016/j.apcato.2024.206975.
[9] X. Li, J. Li, G. Zhang, W. Yang, L. Yang, Y. Shen, Y. Sun, F. Dong, Enhanced reactant activation and transformation for efficient photocatalytic acetone degradation on SnO_2 via Hf doping, Adv. Sustain. Syst. 5 (2021) 2100115, https://doi.org/10.1002/adsu.202100115.
[10] M. Dan-Hardi, C. Serre, T. Frot, L. Rozes, G. Maurin, C. Sanchez, G. Férey, A new photoactive crystalline highly porous titanium(IV) dicarboxylate, J. Am. Chem. Soc. 131 (2009) 10857–10859, https://doi.org/10.1021/ja903726m.
[11] H. Assi, G. Mouchaham, N. Steunou, T. Devic, C. Serre, Titanium coordination compounds: from discrete metal complexes to metal–organic frameworks, Chem. Soc. Rev. 46 (2017) 3431–3452, https://doi.org/10.1039/C7CS00001D.
[12] J. Liu, H. Wang, H. Wu, Y. Yang, C. Wang, Q. Wang, B. Jia, J. Zheng, Research progress on zinc oxide-based heterojunction photocatalysts, J. Mater. Chem. A (2024), https://doi.org/10.1039/D4TA03901G.
[13] Z. Li, Z. Zhou, J. Ma, Y. Li, W. Peng, G. Zhang, F. Zhang, X. Fan, Hierarchical photocatalyst of In_2S_3 on exfoliated MoS2 nanosheets for enhanced visible-light-driven Aza-Henry reaction, Appl. Catal. B 237 (2018) 288–294, https://doi.org/10.1016/j.apcatb.2018.05.087.
[14] N. Tian, C. Hu, J. Wang, Y. Zhang, T. Ma, H. Huang, Layered bismuth-based photocatalysts, Coord. Chem. Rev. 463 (2022) 214515, https://doi.org/10.1016/j.ccr.2022.214515.
[15] B. Zhao, W. Zhong, F. Chen, P. Wang, C. Bie, H. Yu, High-crystalline g-C_3N_4 photocatalysts: synthesis, structure modulation, and H_2-evolution application, Chin. J. Catal. 52 (2023) 127–143, https://doi.org/10.1016/S1872-2067(23)64491-2.
[16] Y. Song, Z. Li, P. Ji, M. Kaufmann, X. Feng, J.S. Chen, C. Wang, W. Lin, Metal–organic framework nodes support single-site nickel(II) hydride catalysts for the hydrogenolysis of aryl ethers, ACS Catal. 9 (2019) 1578–1583, https://doi.org/10.1021/acscatal.8b04611.

[17] B. Kim, Y.-R. Lee, H.-Y. Kim, W.-S. Ahn, Adsorption of volatile organic compounds over MIL-125-NH_2, Polyhedron 154 (2018) 343–349, https://doi.org/10.1016/j.poly.2018.08.010.
[18] H. Wang, X. Yuan, Y. Wu, G. Zeng, H. Dong, X. Chen, L. Leng, Z. Wu, L. Peng, In situ synthesis of In_2S_3@MIL-125(Ti) core–shell microparticle for the removal of tetracycline from wastewater by integrated adsorption and visible-light-driven photocatalysis, Appl. Catal. B 186 (2016) 19–29, https://doi.org/10.1016/j.apcatb.2015.12.041.
[19] C.T. Saouma, S. Richard, S. Smolders, M.F. Delley, R. Ameloot, F. Vermoortele, D. E. De Vos, J.M. Mayer, Bulk-to-surface proton-coupled electron transfer reactivity of the metal–organic framework MIL-125, J. Am. Chem. Soc. 140 (2018) 16184–16189, https://doi.org/10.1021/jacs.8b09120.
[20] N.G. Altınçekiç, C.W. Lander, A. Roslend, J. Yu, Y. Shao, H. Noh, Electrochemically determined and structurally justified thermochemistry of H atom transfer on Ti-oxo nodes of the colloidal metal–organic framework Ti-MIL-125, J. Am. Chem. Soc. 146 (2024) 33485–33498, https://doi.org/10.1021/jacs.4c10421.
[21] J.L. Mancuso, K. Fabrizio, C.K. Brozek, C.H. Hendon, On the limit of proton-coupled electronic doping in a Ti(IV)-containing MOF, Chem. Sci. 12 (2021) 11779–11785, https://doi.org/10.1039/D1SC03019A.
[22] J.L. Mancuso, A.M. Mroz, K.N. Le, C.H. Hendon, Electronic structure modeling of metal–organic frameworks, Chem. Rev. 120 (2020) 8641–8715, https://doi.org/10.1021/acs.chemrev.0c00148.
[23] Y. Guo, C. Hu, Heterogeneous photocatalysis by solid polyoxometalates, J. Mol. Catal. A: Chem. 262 (2007) 136–148, https://doi.org/10.1016/j.molcata.2006.08.039.
[24] K. Suzuki, N. Mizuno, K. Yamaguchi, Polyoxometalate photocatalysis for liquid-phase selective organic functional group transformations, ACS Catal. 8 (2018) 10809–10825, https://doi.org/10.1021/acscatal.8b03498.
[25] L. Jiao, Y. Dong, X. Xin, L. Qin, H. Lv, Facile integration of Ni-substituted polyoxometalate catalysts into mesoporous light-responsive metal-organic framework for effective photogeneration of hydrogen, Appl. Catal. B 291 (2021) 120091, https://doi.org/10.1016/j.apcatb.2021.120091.
[26] L. Bromberg, T.A. Hatton, Aldehyde-alcohol reactions catalyzed under mild conditions by chromium(III) terephthalate metal organic framework (MIL-101) and phosphotungstic acid composites, ACS Appl. Mater. Interfaces 3 (2011) 4756–4764, https://doi.org/10.1021/am201246d.
[27] S. Abednatanzi, K. Leus, P.G. Derakhshandeh, F. Nahra, K. De Keukeleere, K. Van Hecke, I. Van Driessche, A. Abbasi, S.P. Nolan, P.V. Der Voort, POM@IL-MOFs – inclusion of POMs in ionic liquid modified MOFs to produce recyclable oxidation catalysts, Catal. Sci. Technol. 7 (2017) 1478–1487, https://doi.org/10.1039/C6CY02662A.
[28] C.J. Clark, D. Hall, Dodecamolybdophosphoric acid *circa* 30-hydrate, Acta Crystallogr. B Struct. Sci. 32 (1976) 1545–1547, https://doi.org/10.1107/S0567740876005748.
[29] S. Yang, J. Yu, G. Lu, G. Song, G. Shi, Y. Wang, X. Xie, H. Yuan, X. Ren, J. Sun, Effect of NH_2-functionalization of MIL-125 on photocatalytic degradation of o-xylene and acetaldehyde, Chem. Eng. J. 498 (2024) 155251, https://doi.org/10.1016/j.cej.2024.155251.
[30] X.-M. Cheng, X.-Y. Dao, S.-Q. Wang, J. Zhao, W.-Y. Sun, Enhanced photocatalytic CO_2 reduction activity over NH_2-MIL-125(Ti) by facet regulation, ACS Catal. 11 (2021) 650–658, https://doi.org/10.1021/acscatal.0c04426.
[31] S. Naghdi, A. Cherevan, A. Giesriegl, R. Guillet-Nicolas, S. Biswas, T. Gupta, J. Wang, T. Haunold, B.C. Bayer, G. Rupprechter, M.C. Toroker, F. Kleitz, D. Eder, Selective ligand removal to improve accessibility of active sites in hierarchical MOFs for heterogeneous photocatalysis, Nat. Commun. 13 (2022) 282, https://doi.org/10.1038/s41467-021-27775-7.
[32] X. Chang, X.-F. Yang, Y. Qiao, S. Wang, M.-H. Zhang, J. Xu, D.-H. Wang, X.-H. Bu, Confined heteropoly blues in defected Zr-MOF (Bottle Around Ship) for high-efficiency oxidative desulfurization, Small 16 (2020) 1906432, https://doi.org/10.1002/smll.201906432.
[33] Y. Sun, H. Ji, Y. Sun, G. Zhang, H. Zhou, S. Cao, S. Liu, L. Zhang, W. Li, X. Zhu, H. Pang, Synergistic effect of oxygen vacancy and high porosity of nano MIL-125 (Ti) for enhanced photocatalytic nitrogen fixation, Angew. Chem. Int. Ed. (2023) e202316973, https://doi.org/10.1002/anie.202316973.
[34] M.-G. Kim, J. Jeong, Y. Choi, J. Park, E. Park, C.-H. Cheon, N.-K. Kim, B.K. Min, W. Kim, Synthesis of V-doped In_2O_3 nanocrystals via digestive-ripening process and their electrocatalytic properties in CO_2 reduction reaction, ACS Appl. Mater. Interfaces 12 (2020) 11890–11897, https://doi.org/10.1021/acsami.9b19584.
[35] Z. Sun, Y. Hu, J. Zhang, N. Zhou, M. Li, H. Liu, B. Huo, M. Chao, K. Zeng, Interfacial oxygen bridge bonding with Mo-O-Ti units in MoOx@Ti_3C_2 MXene harness efficient Li-O_2 Battery at high rate, Appl. Catal. B 351 (2024) 123984, https://doi.org/10.1016/j.apcatb.2024.123984.
[36] S. Amthor, S. Knoll, M. Heiland, L. Zedler, C. Li, D. Nauroozi, W. Tobaschus, A. K. Mengele, M. Anjass, U.S. Schubert, B. Dietzek-Ivanšić, S. Rau, C. Streb, A photosensitizer–polyoxometalate dyad that enables the decoupling of light and dark reactions for delayed on-demand solar hydrogen production, Nat. Chem. 14 (2022) 321–327, https://doi.org/10.1038/s41557-021-00850-8.
[37] Y. He, Y. Wang, J. Qian, K. Xu, B. Lu, S. Tang, Y. Liu, J. Shen, Efficient photocatalytic H_2O_2 production and green oxidation of glycerol over a $SrCoO_3$-incorporated catalyst, Appl. Catal. B 361 (2025) 124565, https://doi.org/10.1016/j.apcatb.2024.124565.
[38] T. Devic, C. Serre, High valence 3p and transition metal based MOFs, Chem. Soc. Rev. 43 (2014) 6097–6115, https://doi.org/10.1039/C4CS00081A.
[39] A. Vimont, J.-M. Goupil, J.-C. Lavalley, M. Daturi, S. Surblé, C. Serre, F. Millange, G. Férey, N. Audebrand, Investigation of acid sites in a zeotypic giant pores chromium(III) carboxylate, J. Am. Chem. Soc. 128 (2006) 3218–3227, https://doi.org/10.1021/ja056906s.
[40] Y. Han, L. Ye, T. Gong, X. Lu, Y. Fu, Porous Composite-mediated bimetallic cluster POMs/Zr-MOF for catalytic transfer hydrogenation of biomass-derived aldehydes and ketones, Adv. Funct. Mater. (2024) 2315044, https://doi.org/10.1002/adfm.202315044.
[41] M. De Miguel, F. Ragon, T. Devic, C. Serre, P. Horcajada, H. García, Evidence of photoinduced charge separation in the metal-organic framework MIL-125(Ti)-NH_2, ChemPhysChem 13 (2012) 3651–3654, https://doi.org/10.1002/cphc.201200411.
[42] K. Suzuki, N. Mizuno, K. Yamaguchi, Polyoxometalate photocatalysis for liquid-phase selective organic functional group transformations, ACS Catal. 8 (2018) 10809–10825, https://doi.org/10.1021/acscatal.8b03498.
[43] Q. Ruan, M.K. Bayazit, V. Kiran, J. Xie, Y. Wang, J. Tang, Key factors affecting photoelectrochemical performance of g-C_3N_4 polymer films, Chem. Commun. 55 (2019) 7191–7194, https://doi.org/10.1039/C9CC03084K.
[44] B. Yan, Q. Ruan, S. Wang, L. Kong, P. Zhang, H. Wang, Z. Sun, Expediting photo-charging of semiconductors through a bipolar charge storage junction for responsive dark photocatalysis, Adv. Funct. Mater. (2024) 2408895, https://doi.org/10.1002/adfm.202408895.
[45] X. Ruan, X. Cui, Y. Cui, X. Fan, Z. Li, T. Xie, K. Ba, G. Jia, H. Zhang, L. Zhang, W. Zhang, X. Zhao, J. Leng, S. Jin, D.J. Singh, W. Zheng, Favorable energy band alignment of TiO_2 ANatase/rutile Heterophase Homojunctions Yields Photocatalytic Hydrogen Evolution with Quantum Efficiency Exceeding 45.6, Adv. Energy Mater. 12 (2022) 2200298, https://doi.org/10.1002/aenm.202200298.
[46] Z. Rao, G. Lu, L. Chen, A. Mahmood, G. Shi, Z. Tang, X. Xie, J. Sun, Photocatalytic oxidation mechanism of Gas-Phase VOCs: Unveiling the role of holes, •OH and $\bullet O_2^-$, Chem. Eng. J. 430 (2022) 132766 https://doi.org/10.1016/j.cej.2021.132766.
[47] M. Chen, X. Wei, L. Zhao, Y. Huang, S. Lee, W. Ho, K. Chen, Novel N/carbon quantum dot modified MIL-125(Ti) composite for enhanced visible-light photocatalytic removal of NO, Ind. Eng. Chem. Res. 59 (2020) 6470–6478, https://doi.org/10.1021/acs.iecr.9b06816.
[48] A. Jordan, S. Haidacher, G. Hanel, E. Hartungen, L. Märk, H. Seehauser, R. Schottkowsky, P. Sulzer, T.D. Märk, A high resolution and high sensitivity proton-transfer-reaction time-of-flight mass spectrometer (PTR-TOF-MS), Int. J. Mass Spectrom. 286 (2009) 122–128, https://doi.org/10.1016/j.ijms.2009.07.005.
[49] R. Pietro, C. Luca, S. Luigi, L. Ruirui, E. Stefano, M. Gabriele, G. Sebastiano, M. Luca, I. Plinio, M. Xiaojie, W. Bo, Elucidating charge-transfer mechanisms and their effect on the light-induced reactivity of metastable MIL-125(Ti), Appl. Catal. B 345 (2024) 123692, https://doi.org/10.1016/j.apcatb.2024.123692.